Journal of Zhejiang University-SCIENCE A 2026 27(3):288-305
www.jzus.zju.edu.cn; www.springer.com/journal/11582
E-mail: jzus_a@zju.edu.cn

Research Article
https://doi.org/10.1631/jzus.A2500360

Check for updates

Deep-learning-enabled automatic gene abnormality detection via fluorescence in situ hybridization

Lemin SHI[1], Yuqiang ZHANG[2], Haoyu QI[3], Chengyue LU[4], Menglei HU[5], Mingye LI[6], Dianxin SONG[1], Hao ZHANG[1], Xin FENG[1✉], Ping GONG[1✉], Shan JIANG[3✉]

[1]*School of Computer Science and Technology, School of Life Science and Technology, Changchun University of Science and Technology, Changchun 130022, China*
[2]*Modern Industry College, Jilin Jianzhu University, Changchun 130119, China*
[3]*Hangzhou Institute of Technology, Xidian University, Hangzhou 311231, China*
[4]*Department of Electromechanical Engineering, Centre for Artificial Intelligence and Robotics, University of Macau, Macau 999078, China*
[5]*Department of Electrical and Computer Engineering, The University of British Columbia, Vancouver V6T 1Z4, Canada*
[6]*School of Computing and Information Systems, The University of Melbourne, Parkville 3010, Australia*

Abstract: Fluorescence in situ hybridization (FISH) is widely used for diagnosing cancer and genetic disorders due to its high specificity and accuracy. However, traditional methods face challenges such as suboptimal focus adjustments, subjective signal counting errors, and inefficiencies in imaging, limiting their use in high-throughput screening. To address these issues, we introduced the integrated FISH imaging and analysis system (FAST), an innovative solution that combines rapid filter switching, automated focusing, multilayer fluorescence signal fusion, and the improved ResNet152 deep learning framework. Compared with clinical manual counts and analysis of case reports of 10 patients with chronic lymphocytic leukemia (CLL), the FAST achieved an average nuclei segmentation accuracy of 98.28%. For abnormal gene detection, the model achieved an accuracy of 97.86%. Additionally, its intuitive interface allows the operator to complete the entire workflow—from scanning to report generation—within 45 min. FAST represents a significant advancement in cancer and genetic disorder diagnostics, offering a powerful tool for early detection.

Key words: Fluorescence in situ hybridization (FISH); Image enhancement; Nuclei segmentation; Fluorescence feature fusion; Abnormal gene classification

1 Introduction

Cancer remains a leading global health challenge, with rising incidence and mortality emphasizing the urgent need for effective early detection and diagnosis (Siegel et al., 2024). To detect related chromosomal abnormalities, fluorescence in situ hybridization (FISH) has been developed and widely used due to its high specificity and sensitivity (Patino, 2024). Specifically, by using fluorescently labeled probes that hybridize with target deoxyribonucleic acid (DNA) sequences, FISH enables precise visualization of genetic alterations, such as the deletions in 13q14 (Cui et al., 2024), 11q (Krayem et al., 2024), 13q (Knöll et al., 2024), and 17p (Lankford et al., 2024), which are critical for cancer diagnosis, prognosis, and treatment planning (Siegel et al., 2023; Tao et al., 2023). However, as a microscopy-based technique, FISH inherently depends on imaging systems for signal detection and analysis, making its performance closely tied to the quality and efficiency of the microscopy technologies used (Li et al., 2024). For example, the commonly used wide-field fluorescence microscopy provides faster image acquisition by capturing larger sample areas simultaneously (Schermelleh et al., 2019). However, its susceptibility to artifacts (such as halos, low contrast, and uneven staining) can compromise

✉ Xin FENG, fengxin@cust.edu.cn
Ping GONG, gp@cust.edu.cn
Shan JIANG, jiangshan@xidian.edu.cn
Xin FENG, https://orcid.org/0000-0002-8430-1980
Ping GONG, https://orcid.org/0009-0000-0850-3196
Shan JIANG, https://orcid.org/0000-0002-1424-6605

Received July 29, 2025; Revision accepted Nov. 1, 2025;
Crosschecked Jan. 20, 2026; Online first Mar. 11, 2026

the accuracy of fluorescent signal detection (Lewis et al., 2021). These imaging limitations hinder the critical steps of FISH, such as nuclei segmentation and abnormality identification, thereby increasing the likelihood of diagnostic errors (Scott et al., 2018; Nasir et al., 2023). Moreover, the manual and expertise-dependent nature of traditional FISH workflows increases operational complexity, making the process labor-intensive, time-consuming, and prone to subjectivity (Syrykh et al., 2025). Collectively, these challenges limit the scalability and clinical adoption of FISH in high-throughput and rapid diagnostics (Jonkman et al., 2020; Zhang et al., 2021), highlighting the urgent need for innovative solutions to enhance automation, accuracy, and efficiency.

Recent advancements in artificial intelligence (AI) offer transformative opportunities to overcome the challenges associated with traditional FISH analysis. By automating image analysis, AI significantly reduces reliance on manual expertise (Plass et al., 2023), enhances diagnostic accuracy, and enables high-throughput and standardized workflows (Perez-Lopez et al., 2024). Despite its promise, the application of AI in FISH-based genetic diagnostics still faces several critical limitations. These include the insufficient robustness of existing models when confronted with complex genomic backgrounds (Huber et al., 2018; Ordoñez et al., 2024), the need for improved accuracy and efficiency in multi-target detection, the lack of integrated platforms capable of real-time image processing and analysis, and the limited interpretability and clinical usability of current AI systems, which remain below the standards required for routine clinical adoption.

To address these issues, in this paper, we introduce an innovative integrated FISH imaging and analysis system (FAST), which is designed to improve the diagnostic efficiency and reliability of FISH technology under complex imaging conditions. The system integrates a motorized fluorescence microscope (BX61, Olympus Corporation, Japan) with AI-enabled analytical algorithms and a grayscale camera chosen for its superior sensitivity and quantum efficiency (Otomo et al., 2024). Specifically, three key innovations underpin the FAST platform: 1) a multilayer focal plane imaging strategy, which enables comprehensive acquisition across different focal depths to ensure complete cellular structural information, minimize information loss from single-plane imaging, and reduce subjective errors associated with manual focusing. 2) An image enhancement and fusion module, which uses multi-scale filtering and illumination compensation to automatically correct uneven lighting, enhances contrast between nuclear regions and background, and suppresses noise and artifacts. This ensures consistently high image quality even under low-light or complex imaging conditions. 3) An optimized cell nucleus segmentation algorithm, which combines gradient mapping, convex defect detection, and an improved watershed method to achieve highly accurate and robust segmentation, with an average segmentation accuracy of 98.28%, outperforming both traditional and deep-learning-based methods.

The system's gene abnormality detection results show high consistency with expert manual interpretation accuracy of 97.86% and demonstrate robust generalizability in real clinical validation. Moreover, the workflow is fully automated, from sample scanning to diagnostic report generation, greatly enhancing analytical efficiency and reducing reliance on operator expertise. The system features an intuitive and user-friendly interface designed for diverse user groups while maintaining professional oversight for final report verification. Collectively, the FAST platform enables scalable and automated genetic analysis across diverse cancer types and clinical applications, representing a significant advancement in precision oncology and genetic diagnostics.

2 Methods

2.1 Overview of the FAST

Fig. 1 illustrates the overall workflow of the FAST (Fig. S1a of the electronic supplementary materials (ESM)), which comprises three key steps: (I) imaging performance evaluation and acquisition, (II) multiplexed and multilayer image processing, and (III) AI-driven detection of cellular abnormalities. In this study, chronic lymphocytic leukemia (CLL) was chosen as the model disease for system validation due to its relevance to various cancers and operational stability. To highlight the motivation for system development, Fig. 1a summarizes the advantages (Table S1 of the ESM) and limitations (Table S2 of the ESM) of conventional fluorescence microscopy.

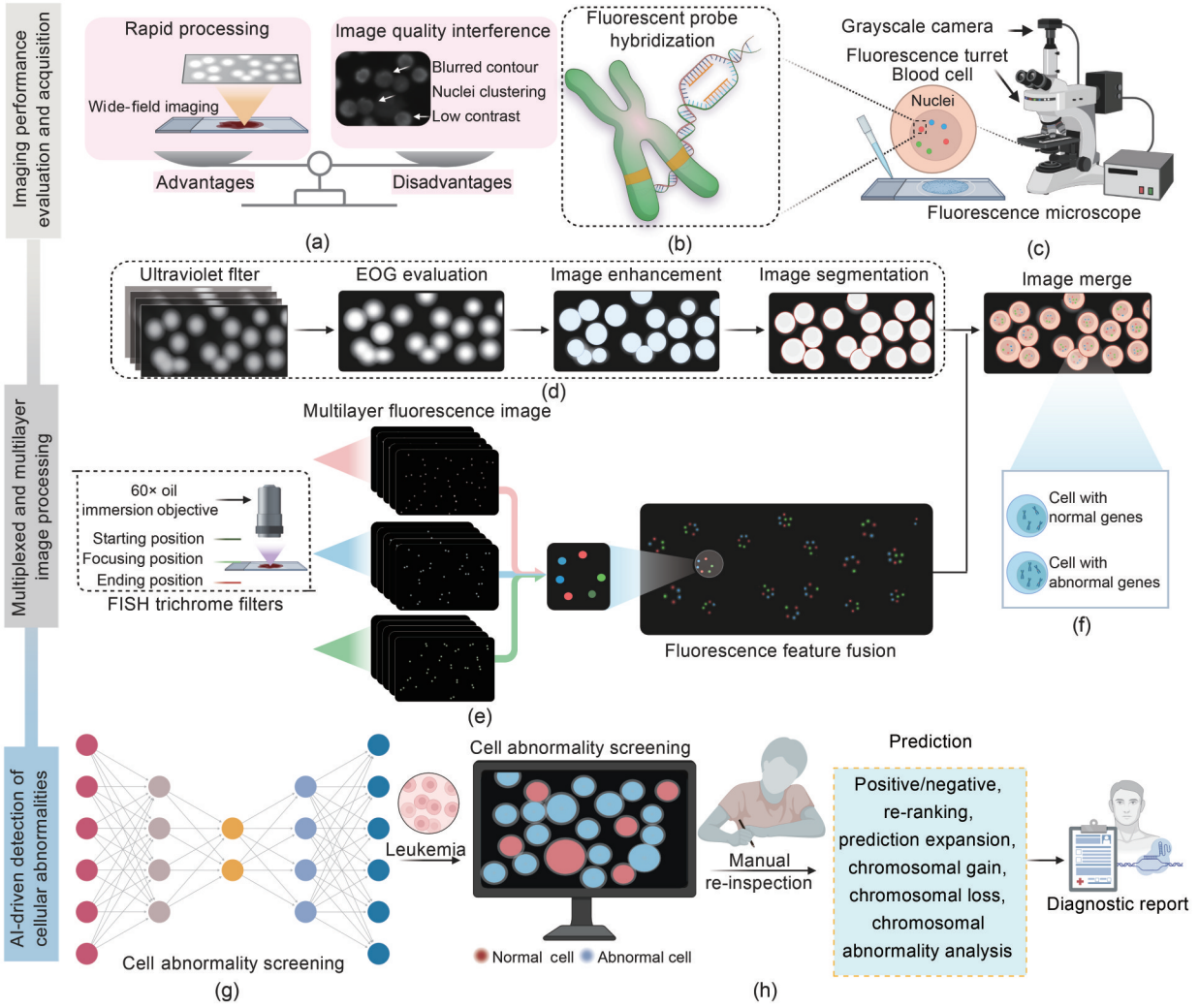

Fig. 1 FAST workflow for cancer diagnosis: (a) overview of the advantages and disadvantages of conventional fluorescence microscopy; (b) FISH probe hybridization targeting specific genetic sequences; (c) image acquisition of hybridized samples using a motorized 2D fluorescence microscope with a grayscale camera, capturing multilayer images through three-color fluorescence filters; (d) image enhancement and segmentation of 4′,6-diamidino-2-phenylindole (DAPI)-stained nuclei to extract clear nuclear contours; (e) fusion and analysis of multilayer fluorescence signals (orange, blue, and green) visualized through tricolor FISH channels; (f) comprehensive cytogenetic data integration from all channels, enabling accurate identification and classification of chromosomal abnormalities; (g) tailored convolutional neural network (CNN) model in the dataset for automated cell abnormality classification; (h) accurate and efficient cancer diagnosis with a user-friendly diagnostic report. EOG is the energy orientation gradient

In Step I, using blood samples collected from suspected CLL patients (Table S3 of the ESM), FAST specifically targets the prevalent 13q14 deletion in this highly genetically heterogeneous cancer (Skerget et al., 2024). To identify cytogenetic markers associated with CLL, the samples were pretreated with DAPI (Xie et al., 2024) for cell interphase nucleus localization. Tricolor XL FISH probes (MetaSystems Probes, Germany) targeting retinoblastoma 1 (RB1, green-ch1), deleted in lymphocytic leukemia 1 (DLEU1, orange-ch3), and lysosomal-associated membrane protein 1 (LAMP1, blue-ch2) were then applied to label the corresponding DNA fragments (Figs. 1b and S1b, as well as Table S4 of the ESM). During image acquisition, each slide was scanned across 36 distinct fields of view, with the system automatically selecting the field containing the highest cell density. The tetrachromatic optical filters switched automatically to acquire multilayer grayscale images at 11 focal depths (102.2–106.6 μm), thereby ensuring optimal axial resolution and signal clarity (Fig. 1c and Section S1 of the ESM).

In Step II, image processing focuses on extracting nuclear contours and fluorescence probe signals. Each sample generates 44 images (four channels multiplied by 11 scanned layers, as shown in Fig. S1c of the ESM). Among these, the image with the highest clarity is selected, and the nuclear contours are segmented (Fig. 1d and Section S2 of the ESM). In parallel, fluorescence features from the orange, blue, and green channels are processed and fused into the segmented images (Fig. 1e). Finally, the nuclear contours and fluorescence information are merged to localize and analyze the signals (Fig. 1f).

In Step III, a CNN model is used to detect chromosomal abnormality in individual cells for CLL diagnosis (Fig. 1g). Synergistically, this automated and multiplexed FAST enables novice operators to rapidly, accurately, and cost-effectively visualize and evaluate cytogenetic features (including deletions and qualitative assessments). Empowered by AI-driven algorithms, FAST achieves precise and reliable detection of chromosomal abnormalities, markedly enhancing diagnostic accuracy. The system features an intuitive and user-friendly interface that streamlines conventional FISH workflows by integrating image acquisition, signal processing, and result interpretation within a unified platform. Through the incorporation of deep learning algorithms, FAST automates nucleus segmentation, fluorescence signal fusion, and abnormality detection, thereby minimizing human error and inter-operator variability. The platform also supports batch automated processing, which significantly improves analytical throughput and reproducibility. Ultimately, FAST generates a comprehensive diagnostic report that undergoes expert manual review for confirmation and quality assurance (Fig. 1h). By combining multiplexed fluorescence imaging with optimized microscopy protocols, this platform shows substantial potential for early cancer detection, prognostic evaluation, and clinical management across diverse cancer types, including cervical cancer (Zhong et al., 2023), pancreatic cancer (Zhao et al., 2023), lung cancer (Elkrief et al., 2024), liver cancer (Sun et al., 2023), breast cancer (Hu et al., 2023), and leukemia (Teierle et al., 2023). In this study, experimental validation was performed using a CLL dataset, and all results were manually verified and confirmed by certified cytogenetics experts.

2.2 Image enhancement and nucleus segmentation

Image enhancement was conducted using the multi-scale Retinex32 algorithm and an image fusion model. Each image consists of two components: irradiation and reflection (Sun et al., 2022). The irradiation component represents the low-frequency part, while the reflection component contains the high-frequency details. Based on the EOG algorithm (Choudhary and Sethi, 2023), the optimal gradient energy image $I(x, y)$ can be obtained as:

$$I(x,y) = L(x,y) \times R(x,y), \tag{1}$$

where x and y are the x- and y-coordinates of the image pixel, respectively; $L(x, y)$ and $R(x, y)$ are the irradiation component and reflection component, respectively.

High-frequency details are extracted via multi-scale Gaussian filtering (Sheng et al., 2025). The globally enhanced image is first convolved with Gaussian kernels with different standard deviations (G_1=1.0, G_2=2.0, and G_3=3.0), generating three blurred images. The corresponding contour details are then computed as follows:

$$\begin{cases} L_i' = G_i \times L(x,y), \\ D_i = L_i' - L_{i+1}', \end{cases} \tag{2}$$

where L_i' (i=1, 2, 3) is the blurred image at scale i; G_i is the Gaussian kernel with standard deviation; D_i is the high-frequency detail image between adjacent scales.

To prevent oversaturation while preserving image structure, a fusion model combines multi-scale details:

$$D^* = [1 - \omega_1 \times \mathrm{sgn}(D_1)] \times D_1 + \omega_2 \times D_2 + \omega_3 \times e \times D_3, \tag{3}$$

where D^* is the overall contour information fused across scales; ω_1, ω_2, and ω_3 denote the image clarity at each scale (computed via the Laplacian operator); $\mathrm{sgn}(D_1)$ is the sign function of D_1; e is the empirical parameter. An empirical parameter e=0.1 controls the retention of original image content, achieving a balance between detail enhancement and natural appearance. This approach effectively enhances FISH and other microscopic images, yielding superior visual quality through multi-scale detail fusion.

Gaussian high-pass filtering is applied to the enhanced reflection components $R'(x, y)$ in the frequency domain, and the filter is defined as:

$$R'(x,y) = I(x,y) + D^*, \tag{4}$$

$$H(u,v) = 1 - \mathrm{e}^{-\frac{D^2(u,v)}{2\times D_0^2}}, \tag{5}$$

where u and v are the frequency coordinates in the horizontal and vertical directions, respectively; $H(u,v)$ is the Gaussian high-pass filter; $D(u,v)$ is the distance between the frequency point (u,v) and the center of the frequency domain; D_0 is the cutoff frequency controlling the filter bandwidth.

To precisely adjust highlights while maintaining balanced exposure and detail, the top 0.1% of brightness values—representing key highlight regions—are selectively processed. This targeted adjustment enhances image quality and preserves essential information without overexposure.

$$H'(u,v) = C_{\mathrm{oe}} \times H(u,v) + L(x,y), \tag{6}$$

where C_{oe} denotes an overexposure control coefficient used for gain adjustment to suppress excessive highlights.

A Fourier transform is applied to the processed image, and the inverse transform is combined with the incident component $H'(u, v)$. Gain adjustment using C_{oe} prevents overexposure, producing the final enhanced image (Section S3 of the ESM).

2.3 Nuclear morphology prediction and segmentation

The Euclidean distance $D(P,Q)$ between each object pixel $P(x_1, y_1)$ and its nearest background pixel $Q(x_2, y_2)$ is as follows (Shen et al., 2019):

$$D(P,Q) = \sqrt{(x_1 - x_2)^2 + (y_1 - y_2)^2}, \tag{7}$$

where x_1 and y_1 denote the coordinates of an object pixel P; x_2 and y_2 denote the coordinates of its nearest background pixel Q. The set of Euclidean distances $D_s[D(P, Q)]$ computed for all object pixels attains maximum and minimum values, denoted as $D_{\max}$ and $D_{\min}$, respectively.

The spatial distribution of nucleus pixels is converted into grayscale values to form the distance map $G(x, y)$. The converted grayscale values are calculated as follows (Sharma et al., 2022):

$$G(x,y) = 255 \times \frac{|D(P,Q) - D_{\min}|}{|D_{\max} - D_{\min}|}. \tag{8}$$

Local extrema of $G(x, y)$ are identified, their peak coordinates are recorded, and the distances between adjacent peak points are computed as follows (Jardim et al., 2022):

$$D_{\min}(A,B) = \sum_{a=1}^{m}\sum_{b=1}^{n}\sqrt{(x_a - x_b)^2 - (y_a - y_b)^2}, \tag{9}$$

where A and B denote two sets of peak points extracted from the enhanced image; $D_{\min}(A,B)$ denotes the minimum distance between adjacent peak points of two sets A and B; x_a and y_a (a=1, 2, ⋯, m) denote the coordinates of the ath peak point in set A, and m is the number of peak points in A; x_b and y_b (b=1, 2, ⋯, n) denote the coordinates of the bth peak point in set B, and n is the number of peak points in B.

The energy field gradient mapping model highlights nuclear boundaries by analyzing pixel intensity gradients, enhancing edge contrast, and reducing noise-induced false detections. It effectively emphasizes regions with strong intensity variations, reflecting texture and morphological irregularities such as protrusions or indentations.

The enhanced image gradients are computed using the Sobel operator Eq. (9) to obtain magnitude and direction, forming a herpes simplex virus (HSV)-like representation (Dai et al., 2024). The mapping model accentuates nuclear boundaries, enhances regions with strong intensity variations, and accurately defines nuclear contours (Section S4 of the ESM).

For the mapped grayscale image $I_{\mathrm{binary}}(x, y)$, binarization was performed using a global threshold T=10, determined through preliminary edge analysis and Otsu-based calculations. Comparative tests with T=5, 10, and 15 showed that T=10 most effectively separated cell nuclei from the background, minimizing over- and under-segmentation. Thus, T=10 was confirmed as the optimal threshold for generating the final binary image $I_{\mathrm{binary}}(x, y)$:

$$I_{\mathrm{binary}}(x,y) = \begin{cases} 255, & \text{if } I_{\mathrm{gray}}(x,y) > T, \\ 0, & \text{otherwise}, \end{cases} \tag{10}$$

where $I_{\text{gray}}(x,y)$ denotes the grayscale intensity value of the mapped image at pixel location (x,y). To suppress noise, erosion is first applied to I_{binary}, followed by dilation using a 3×3 structural element K with coordinate offset $(\Delta x, \Delta y)$:

$$I_{\text{erode}} = \min_{(\Delta x,\ \Delta y)\ \in K} I_{\text{binary}}(x+\Delta x, y+\Delta y), \quad (11)$$

$$I_{\text{dilate}} = \max_{(\Delta x,\ \Delta y)\ \in K} I_{\text{binary}}(x+\Delta x, y+\Delta y), \quad (12)$$

where Δx and Δy denote the coordinate offsets within the structuring element K, such that $(x+\Delta x, y+\Delta y)$ corresponds to a neighboring pixel coordinate; I_{erode} and I_{dilate} denote erosion and dilation results, respectively, forming a morphological opening that removes noise and smooths boundaries.

The boundaries of all foreground objects are detected by comparing each pixel in the binary image with its eight-neighbor grayscale values. A parent–child contour hierarchy is then constructed for subsequent processing. Finally, the contours are simplified by retaining only key corner points, so the simplified contour set C' preserves the essential shape and hierarchical structure of the image.

Based on the Teh–Chin chain code contour approximation, the least-squares method is employed to fit the contour points by minimizing the total fitting error e_{f}, defined as the vertical distance between the observed point y_j and the fitted curve $f(x_i)$. The optimization process is expressed as:

$$\frac{\partial e_{\text{f}}}{\partial (p_1, p_2)} = -2\sum_{i=1}^{n}\begin{bmatrix} x_i \\ 1 \end{bmatrix}[y_i - (p_1 x_i + p_2)] = 0, \quad (13)$$

where p_1 and p_2 are the optimal parameters of the fitting line obtained by solving the fitting equation.

The resulting line is then used to approximate the original contour point set, producing a smoothed contour set C'', expressed as:

$$C'' = [x_i, f(x_i)],\ i = 1, 2, \cdots, n. \quad (14)$$

Fusing two contour datasets eliminates redundant points and smooths noise while preserving the hierarchical contour structure. This enhances contour detection accuracy and efficiency across images of variable complexity.

$$C_{\text{f}} = C' \cup C'', \quad (15)$$

where C_{f} denotes the final fused contour set obtained by merging the two contour datasets C' and C''. Based on C_{f}, convex defects are identified and visualized through a two-step screening process, ensuring efficient and accurate morphological segmentation, especially for complex nuclear structures.

Step 1: convex defect detection. Within the fused contour dataset C_{f}, regions deviating from the convex hull are identified as convex defects. Significant concave areas are detected by computing the defect depth, defined as the perpendicular distance between the convex hull and the farthest contour point.

Step 2: labeling and filtering defects. Each convex defect in C_{f} is evaluated by comparing its defect depth with a predefined threshold. Defects exceeding this threshold are labeled as significant morphological features and visualized (e.g., using circular markers).

If the line intersects the convex hull, the intersection point $P_i(x_i, y_i)$ is obtained, and the distance $D(P_i, P_p)$ to the corresponding peak point $P_p(x_p, y_p)$ is calculated according to Eq. (16):

$$D(P_i, P_p) = \sum_{i,p}^{m,n} \sqrt{(x_i - x_p)^2 + (y_i - y_p)^2}, \quad (16)$$

where x_i and y_i (i=1, 2, ⋯, m) denote the coordinates of the intersection point between the line and the convex hull; x_p and y_p (p=1, 2, ⋯, n) denote the coordinates of the corresponding peak point.

2.4 Multi-layer fluorescence feature fusion

The EOG algorithm is used to calculate the clarity E_i of each image layer by evaluating the gradient changes in the image.

$$E_i = \frac{1}{M \times N}\sum_{x=1}^{M}\sum_{y=1}^{N}\left[\left|\frac{\partial I_i(x,y)}{\partial x}\right| + \left|\frac{\partial I_i(x,y)}{\partial y}\right|\right], \quad (17)$$

where I_i=(x, y) (i=1, 2, ⋯, L) denotes the pixel intensity of the ith image layer, and L denotes the total number of image layers; M and N denote the width and height of the image, respectively; ∂x and ∂y denote the gradients in the horizontal and vertical directions, respectively.

The image with the highest E_i is selected as the base image $I_{\text{base}}(x, y)$, and the global threshold T is calculated to extract significant fluorescence signals.

$$T=\frac{1}{M\times N}\sum_{x=1}^{M}\sum_{y=1}^{N}I_{\text{base}}(x,y). \tag{18}$$

Using global threshold T, the fluorescence signals are extracted from each image layer to generate binary masks $M_i(x, y)$ (i=1, 2, ⋯, n):

$$M_i(x,y)=\begin{cases}I_{\text{base}}(x,y), & \text{if } I_{\text{base}}(x,y)\geqslant T,\\ 0, & \text{otherwise.}\end{cases} \tag{19}$$

Layer by layer, the extracted signals at the kth layer S_k (k=2, 3, ⋯, n) are sequentially overlaid to obtain the fused image:

$$F_k=F_{k-2}+S_{k-1}+S_k, \tag{20}$$

where F_k (k=3, 4, ⋯, n) denotes the fused image obtained after combining the first k extracted signal layers.

Through this step-by-step fusion, the signal from the 11th layer compensates for the blurred signals from the defocused layers, thereby enhancing the precision and robustness of segmentation. With the increase in n, both image clarity and clear signal ratio progressively improve until n=9. Beyond this point, the improvement reaches a plateau, indicating that n=9 provided an optimal balance between signal compensation and computational efficiency for FISH analysis in this study.

2.5 Deep-learning-based cell abnormality detection for early diagnosis

The ResNet152 architecture (Malik et al., 2024) was selected as the base network owing to its strong generalization capability and compatibility with pretrained models, making it particularly suitable for analyzing the diverse fluorescence patterns and complex backgrounds typical of FISH images. This architecture is especially advantageous in scenarios involving data imbalance or limited sample availability. Compared to lighter architectures, although computationally more demanding, ResNet152 achieves an optimal balance between diagnostic accuracy, robustness, and efficiency, making it the most suitable choice for high-precision FISH-based genetic abnormality detection in this study. By stacking multiple 3×3 convolutional kernels, the receptive field is progressively expanded layer by layer, achieving the same effective coverage as the original 7×7 convolutional kernel. This strategy substantially reduces the number of parameters while maintaining equivalent feature extraction performance.

$$F(i)=F(i+1)+(K_{\text{size}}-1)\times S, \tag{21}$$

where $F(i)$ denotes the receptive field of the ith layer; $F(i+1)$ denotes that of the (i+1)th layer; K_{size} is the size of the convolutional kernel; S is the step size. The specific details are as follows:

Layer 1: the input receptive field parameters are $F(i+1)$=1, K_{size}=3, S=1, and $F(1)$=1+(3−1)×1=3.

Layer 2: the input receptive field parameters are $F(i+1)$=3, K_{size}=3, S=1, and $F(2)$=3+(3−1)×1=5.

Layer 3: the input receptive field parameters are $F(i+1)$=5, K_{size}=3, S=1, and $F(3)$=5+(3−1)×1=7.

The introduction of a multi-branch design replaces the traditional single 7×7 convolutional kernel, enabling each branch to use a 3×3 convolutional kernel. This architecture effectively reduces both the computational load and the number of parameters. By optimizing the network structure, the multi-branch design preserves the receptive field while simultaneously enhancing computational efficiency and reducing the risk of overfitting, resulting in improved model performance and generalization capability.

For the multi-branch design, where each branch uses a 3×3 convolutional kernel, the number $N_{\text{p},3\times3}$ of parameters can be calculated using the formula:

$$N_{\text{p},3\times3}=3\times(C_{\text{in}}\times C_{\text{out}})\times3\times3, \tag{22}$$

where C_{in} is the number of input channels; C_{out} is the number of output channels; 3×3 is the size of the convolution kernel.

The parameter reduction rate R_{pr} for the multi-branch design is given by the formula:

$$R_{\text{pr}}=1-\frac{N_{\text{p},3\times3}}{N_{\text{p},7\times7}}, \tag{23}$$

where $N_{\text{p},7\times7}$ is the number of parameters for the multi-branch design, where each branch uses a 7×7 convolutional kernel.

Global average pooling (GAP) is used instead of the traditional fully connected layer, reducing the number of model parameters and preventing potential

information loss introduced by the flattening operation. GAP computes the global average of each feature channel, directly mapping the 2D feature maps to corresponding global feature values for each class. This design further enhances the computational efficiency, stability, and generalization capability of the model.

In this study, we used an optimized cell nucleus segmentation method to extract cell nuclei from multilayer fluorescence feature fusion images. The segmentation results were reviewed and approved by pathology experts, and about 4500 high-quality nucleus images were screened as the initial sample set. Based on this dataset and incorporating data augmentation strategies, such as image translation, rotation, mirroring, and scaling, a representative and diverse extended dataset comprising 26733 images was constructed. The dataset was then divided into a training set (18713 images) and a validation set (8020 images) with a 7:3 ratio, and the division of homologous images was strictly controlled to avoid information leakage.

For data annotation, images were classified according to the characteristics of the fluorescence signals. Images containing a single fluorescent spot or no detectable fluorescent signal were annotated as abnormal samples (i.e., gene abnormality representation), while images showing two fluorescent spots were annotated as normal samples. All annotation results were reviewed and verified in multiple rounds to ensure label accuracy and consistency. Based on this dataset, a classification model was trained, and the model performance was comprehensively evaluated using multi-dimensional indicators, such as the confusion matrix, accuracy, sensitivity, and specificity, to verify the effectiveness and reliability of the proposed method in abnormal gene classification.

Abnormal cells were detected on 10 sets of trichrome multilayer fluorescence feature-fused images according to the cell morphological integrity and absence threshold relationship criteria. Through the manual operation, 200 cells in each image were selected for detection with a missing proportion threshold of 5%, i.e., 10 abnormal cells per 200 total cells. In cases where the system detects fewer than 200 cells, it calculates the threshold for an abnormal cell count by multiplying the actual cell count by the specified missing proportion threshold. The quantification of fluorescent genetic signals within individual cells using three monomeric fluorescence probes enables the identification and characterization of genetic abnormalities at the cellular level separately, and the number of abnormal cells is compared with the abnormal cell number threshold.

The accuracy A_{cc}, precision P_{re}, recall R_{cc}, and F1-score F_{1s} of the cell abnormality analysis results can be calculated as follows:

$$A_{cc}=\frac{P_T+N_T}{P_T+N_T+N_F+P_F}, \tag{24}$$

$$P_{re}=\frac{P_T}{P_T+P_F}, \tag{25}$$

$$R_{cc}=\frac{P_T}{P_T+N_F}, \tag{26}$$

$$F_{1s}=2\times\frac{(R_c\times P_{re})}{(R_c+P_{re})}, \tag{27}$$

where P_T is the true positive; N_T is the true negative; P_F is the false positive; N_F is the false negative.

The training dataset was imported into different classification models for automated learning and training, using default parameters with a weight decay value of 0.1 and an initial learning rate of 0.001. The model was trained for 20 epochs, and to prevent overfitting, individual neurons in training were selectively ignored using a random discard technique after each fully connected layer. The classification results were output through the classifier. Upon completion of training, the final trained model, including its network structure and optimized parameters, was retrieved. The nine-layer fluorescence fusion images were then imported into different classification models as a dataset. The models were further fine-tuned and optimized using this dataset. Following this, 30% of the images were randomly selected as a test set to evaluate the model's predictive performance, yielding prediction results.

3 Results

3.1 Performance evaluation and comparison in cell nucleus segmentation

Image enhancement in the FAST begins by selecting the optimal EOG image from the DAPI channel (Section S2, Fig. S2, and Table S5 of the ESM). The selected image is then decomposed into low- and

high-frequency components (Fig. 2a). Using a multi-scale difference of Gaussians (DoGs) algorithm (Li XJ et al., 2022), the high-frequency details are isolated to enhance nuclear edges and textural information. The low-frequency is optimized to maximize the signal-to-noise ratio (SNR) for minimized noise. In addition, local contrast factors are extracted from the brightest 0.1% of pixels to enhance low-contrast areas. The final enhanced image simultaneously amplifies high-frequency structural details while preserving low-frequency information, effectively resolving issues such as blurred edges, uneven brightness, and background noise (Fig. S3 of the ESM). Compared with conventional image enhancement methods, such as contrast-limited adaptive histogram equalization (CLAHE) (Hu et al., 2024), single-scale retinex (SSR) (Li et al., 2021), and homomorphic filtering (HF) (Ramos-Soto et al., 2021), the proposed approach shows superior contrast enhancement and noise reduction (Section S4 and Fig. S4 of the ESM).

To achieve accurate and efficient nucleus segmentation, an optimized watershed-based algorithm was developed (Fig. 2b). This process begins with identifying local extrema in the enhanced images as

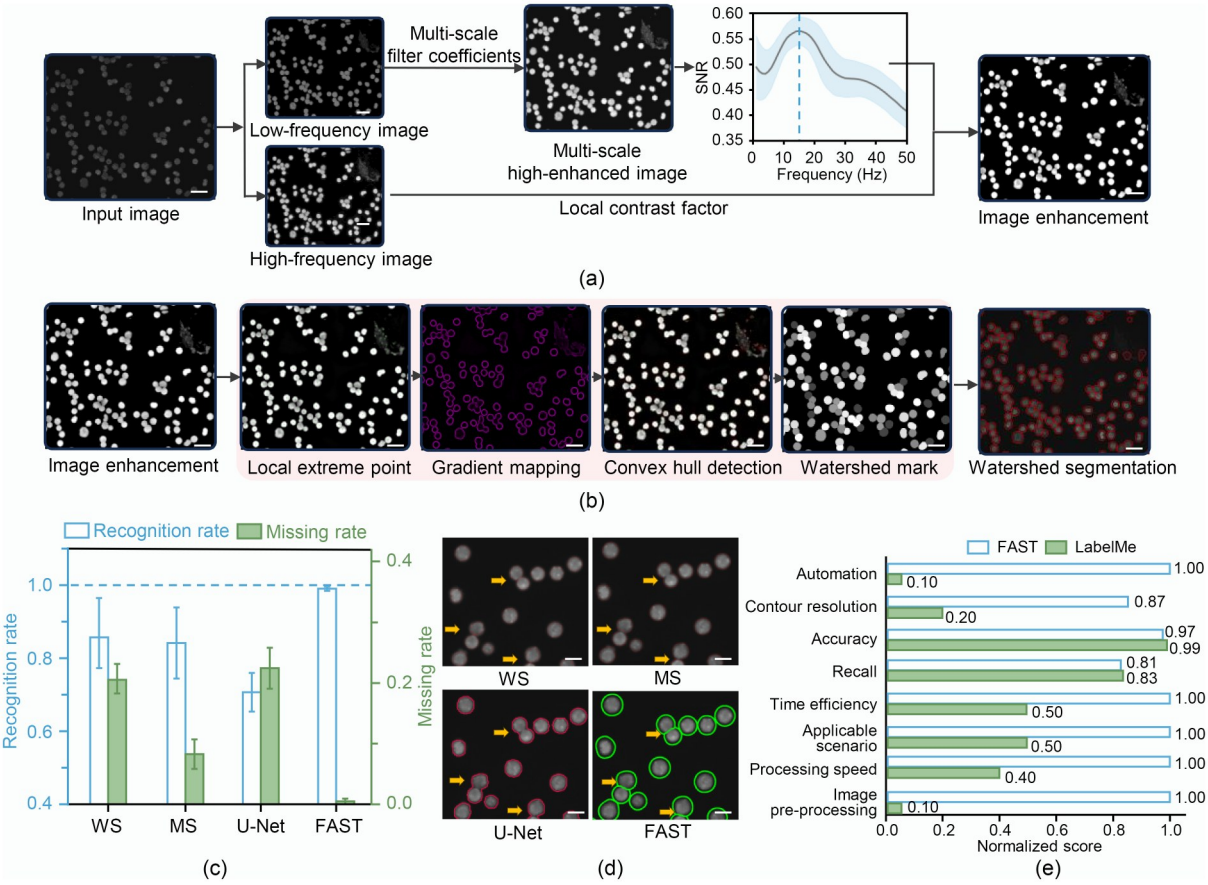

Fig. 2 Image enhancement and nucleus segmentation for accurate nuclear contour identification: (a) workflow of the image enhancement process, with the tailored multi-scale DoGs algorithm and image fusion model improving edge sharpness and contrast while enhancing nuclear contours and details; (b) accurate segmentation of nuclear regions, where representative raw images with complex patterns are processed through local maxima identification, gradient mapping for feature extraction, convex defect analysis for edge detection, and iterative refinement of seed points; (c) performance comparison of nucleus counting accuracy across different segmentation methods; (d) comparative analysis of clustered nucleus segmentation results by our method and other established methods, with orange arrows highlighting segmentation performance on clustered nuclei; (e) comprehensive performance comparison between FAST and LabelMe across key metrics, including automation, accuracy, recall, time efficiency, processing speed, etc. Scale bars: 10 μm in (a) and (b); 5 μm in (d). MW, MS, and U-Net denote marker-based watershed, morphological segmentation, and a commonly used U-Net-based semantic segmentation deep learning method, respectively. LabelMe refers to a commercial manual image annotation tool used as a baseline

seed points, which are refined using Sobel gradients (Wang et al., 2024) and flow field information. The images are then transformed into the HSV color space (Chyad et al., 2025) to improve edge visibility and reduce misidentification (Fig. S5 and Section S5 of the ESM). Further refinement involves a two-pass convex hull detection to address over- and under-segmentation. Moreover, iterative adjustments to watershed mark parameters based on peak distances ensure accurate delineation of individual nucleus, even when there are overlapping and complex backgrounds (Fig. S6 of the ESM). Comparative analysis with traditional methods like MW (Abrol et al., 2023), MS (Vincent and Dougherty, 1994), and U-Net (Punn and Agarwal, 2022) shows that our proposed approach achieves superior segmentation performance (Fig. S7 of the ESM). With an average segmentation accuracy of 98.28% and a missing rate (i.e., the ratio of undetected nuclei to total nuclei) below 2%, the FAST outperformed other traditional methods (accuracy range: 54.8%–82.7%) in counting nuclei (Fig. 2c and Section S6 of the ESM). In scenarios involving tightly packed nuclei, our proposed approach produced clear segmentation results, avoiding over-segmentation and nucleus omission commonly observed in other approaches (Fig. 2d and Section S7 of the ESM).

FAST also exhibits significant advantages in scalability and efficiency compared with commercial solutions like LabelMe. Although both FAST and LabelMe achieved comparable accuracy (0.97 vs. 0.99) and recall (0.81 vs. 0.83), FAST showed superior time efficiency and required fewer computational resources (Fig. 2e and Section S8 of the ESM). Moreover, in contrast to traditional deep learning methods like U-Net (Soltanian-Zadeh et al., 2019; Minaee et al., 2022), FAST's lightweight design reduces dependency on large-scale datasets and high-performance hardware, enabling rapid processing of extensive imaging datasets. This advantage is particularly beneficial for complex nucleus recognition tasks, where FAST efficiently completes the entire workflow from image preprocessing to segmentation.

3.2 Evaluation of multilayer fluorescence feature fusion indicators

In this study, CLL detection focused on key gene regions on chromosome 13 (RB1, DLEU1, and LAMP1) (Durak Aras et al., 2021). To visualize genetic abnormalities, FISH probes labeled with green, orange, and blue fluorescence targeted distinct chromosomal regions, enabling direct microscopic observation (Fig. 3a and Fig. S8 of the ESM). To enhance detection accuracy, a multilayer fluorescence feature fusion strategy was applied to improve fluorescence characteristics within the nuclei (Caicedo et al., 2017). For each fluorescence signal, 11 layers with increasing focal distances were captured and ranked according to their E_i (Fig. 3b). The layer with the highest E_i was selected as the base layer, and fluorescence features from the top n layers (n=1, 3, 5, 7, 9, and 11) were progressively fused into this base, resulting in a pseudo-colored composite image (Fig. 3c and Fig. S9 of the ESM). This multilayer fusion process enhances fluorescence signals and addresses common issues such as information loss and blurriness (Fig. 3d and Fig. S10 of the ESM) (Xu et al., 2023).

To assess image quality, the average accumulated E_i for each signal and the ratio of clear signals were calculated (Section S9 of the ESM). Results show that image quality plateaued after n=9 (Figs. 3e and 3f), indicating that n=9 provided an optimal balance between signal enhancement and processing cost for FISH analysis in this study (Fig. S10 of the ESM). In the fused microscopy images, the fluorescent patterns convey diagnostic information, enabling the distinction of aberrant cells (Fig. 3g). As shown in Fig. 3h, normal cells exhibit two green (2G), two orange (2O), and two blue (2B) signals, whereas aberrant cells show reduced signal patterns, such as 1O, 1G, or 1B. In CLL (Zhang et al., 2024), more than 50% of patients had deletions in the 13q14 region (Saeed et al., 2024).

To statistically determine the optimal fusion depth for tricolor FISH image analysis, six fusion layers (n= 1, 3, 5, 7, 9, and 11) were compared using two quantitative indicators: average accumulated E_i (signal intensity) and clear signal count (signal quality). Ten independent samples were analyzed under identical imaging conditions, and the results were assessed by 95% confidence interval (CI) and one-way analysis of variance (ANOVA) with Tukey's honestly significant difference (HSD) post-hoc tests (significance level α= 0.05). Both metrics stabilized as the fusion depth increased. The average accumulated E_i increased from 8.23 (n=1) to 18.51 (n=9) with narrowing CI, while n=11 showed no further improvement (18.48, CI=

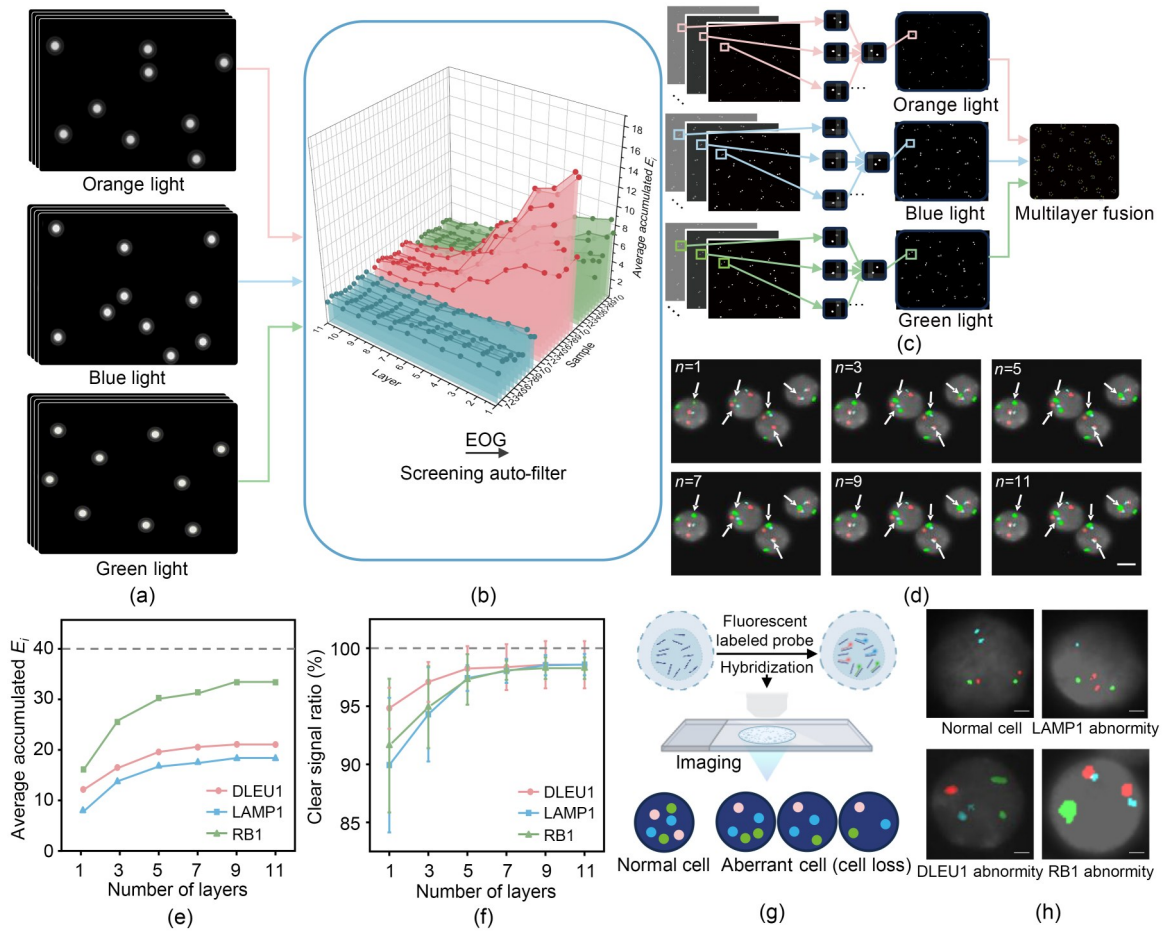

Fig. 3 Multilayer fluorescence feature fusion for chromosomal abnormality screening: (a) FISH images from different channels with specific fluorescent signals; (b) ranking of fluorescence images based on the EOG for signal clarity; (c) automated filtering and multilayer fusion of tricolor fluorescence images; (d) comparison of fluorescence signal restoration through *n*-layer fluorescence feature fusion (*n*=1, 3, 5, 7, 9, and 11), showing a progressive enhancement of fluorescence signals with increasing *n*; (e) and (f) average accumulated E_i and clear signal ratio across *n*-layer feature fusion (*n*=1, 3, 5, 7, 9, and 11); (g) workflow of FISH technology for detecting chromosomal abnormalities in CLL; (h) FISH patterns showing gene deletions in the 13q14 region in CLL patients. Scale bars: 10 μm in (d) and 5 μm in (h)

16.42%–20.54%), indicating signal saturation. Meanwhile, the clear signal count decreased from 25.67 (*n*=1) to 5.60 (*n*=9) as noise was suppressed, but slightly dropped at *n*=11, suggesting minor signal loss. ANOVA confirmed a significant effect of fusion depth on both metrics (E_i: F=21.87 and p<0.001; clear signal count: F=18.42 and p<0.001, where F statistic is the ratio of the between-group variance to the within-group variance, and it is used to test whether there are significant differences among multiple group means). Post-hoc tests showed that low-depth fusions ($n \leqslant 3$) differed markedly from higher-depth ones (p<0.001), while *n*=9 and *n*=11 did not differ in E_i (p=0.982) but differed in signal count (p=0.043). Overall, *n*=9 was the optimal number of image layers, focal depths, or segmentation model hyperparameters across different processing stages. Repeated experimental validation confirmed that *n*=9 provides the most effective trade-off among accuracy, detection capability, and computational efficiency, particularly under diverse and noise-prone imaging conditions.

This method allows accurate detection of chromosomal abnormalities in CLL, providing a crucial foundation for clinical prognosis evaluation. Using the proposed multilayer fluorescence feature fusion approach, an in-depth assessment of chromosomal abnormalities was performed. The average accumulated E_i and chromosomal abnormality ratio (R_{al}) for each

signal were analyzed. As the number of fused layers increased from 1 to 11, the abnormality ratios stabilized, reflecting a gradual enhancement of fluorescence signals (Table S6 of the ESM). To classify cell abnormalities and diagnose cancer, a 5% threshold across the three FISH channels was set (Table S7 of the ESM). Specifically, samples were considered negative if R_{al} values in all channels were below this threshold, and positive otherwise. By applying the multilayer fluorescence feature fusion method, chromosomal abnormalities in 10 independent samples with different n values were further evaluated based on average accumulated E_i measurements (Fig. 4 and Figs. S11–S14 of the ESM). The results show that abnormality classification accuracy improved consistently as n increased, which further strengthened the reliability of FISH analysis. These findings indicate that the proposed method effectively reduces issues, such as halo, blurring, and signal loss, providing a more accurate representation of fluorescence intensity within the nuclei.

3.3 Abnormal gene screening and application based on deep learning

Building upon the multilayer fluorescence feature detection results, a deep learning model based on the ResNet152 backbone was developed to enable automated cell abnormality detection and facilitate early cancer diagnosis (Fig. 5a). In this model, the CNN leverages the robust feature-extraction capability of ResNet152 and is trained using uniformly resized input images (224×224 pixels) with a segmented learning-rate decay strategy (initial rate=0.001). To determine the optimal fusion level, datasets with n-layer fusion (n=1, 3, 5, 7, and 9) were evaluated. Among these, the nine-layer fusion dataset showed the fastest convergence and highest predictive accuracy, striking a balance between information density and task complexity (Fig. 5b). Consequently, the nine-layer fusion dataset was selected for chromosomal and cellular abnormality classification, achieving high accuracy in detecting abnormalities at both levels (Fig. 5c, Fig. S15, and Tables S8–S11 of the ESM). To enhance

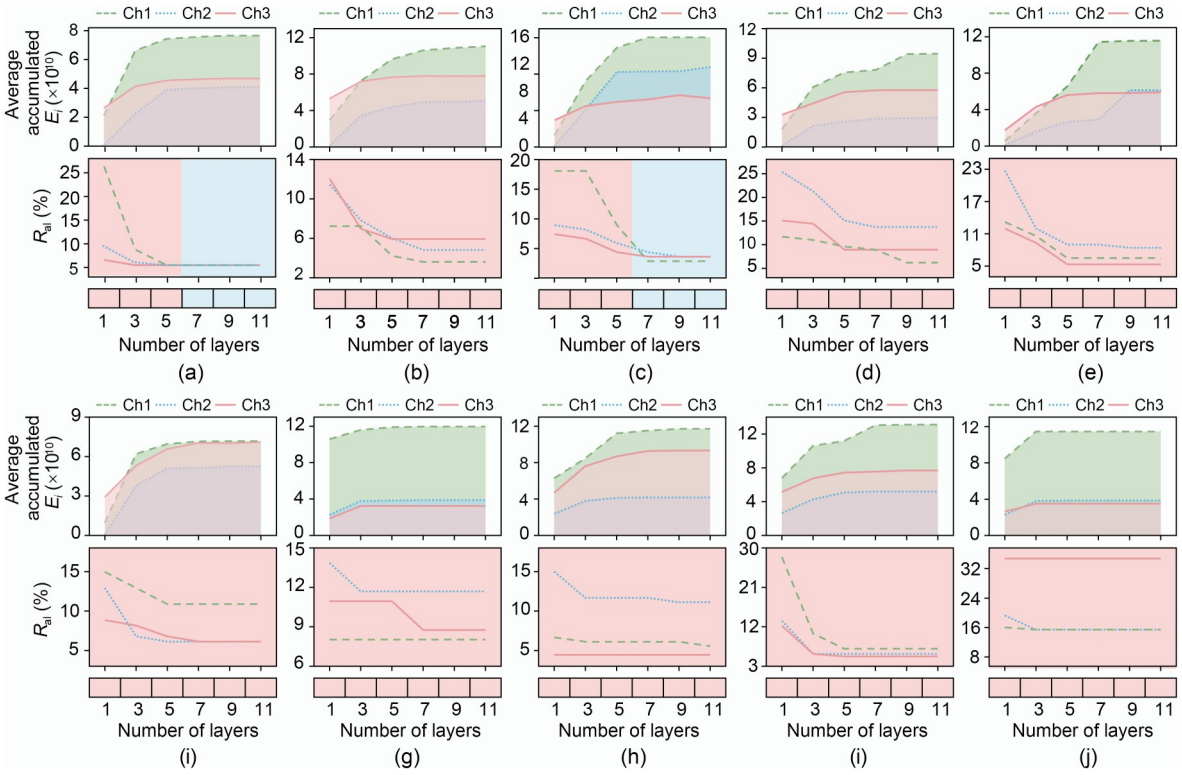

Fig. 4 Evaluation of the specificity of tricolor fluorescence signals against the increase of n: average accumulated E_i and chromosomal abnormality ratio across (a)–(j) sample 1 to sample 10. Areas in the R_{al} plots and shaded cells denote manual classification of chromosomal abnormality and corresponding cell abnormality, respectively, with orange denoting abnormality and blue denoting normality

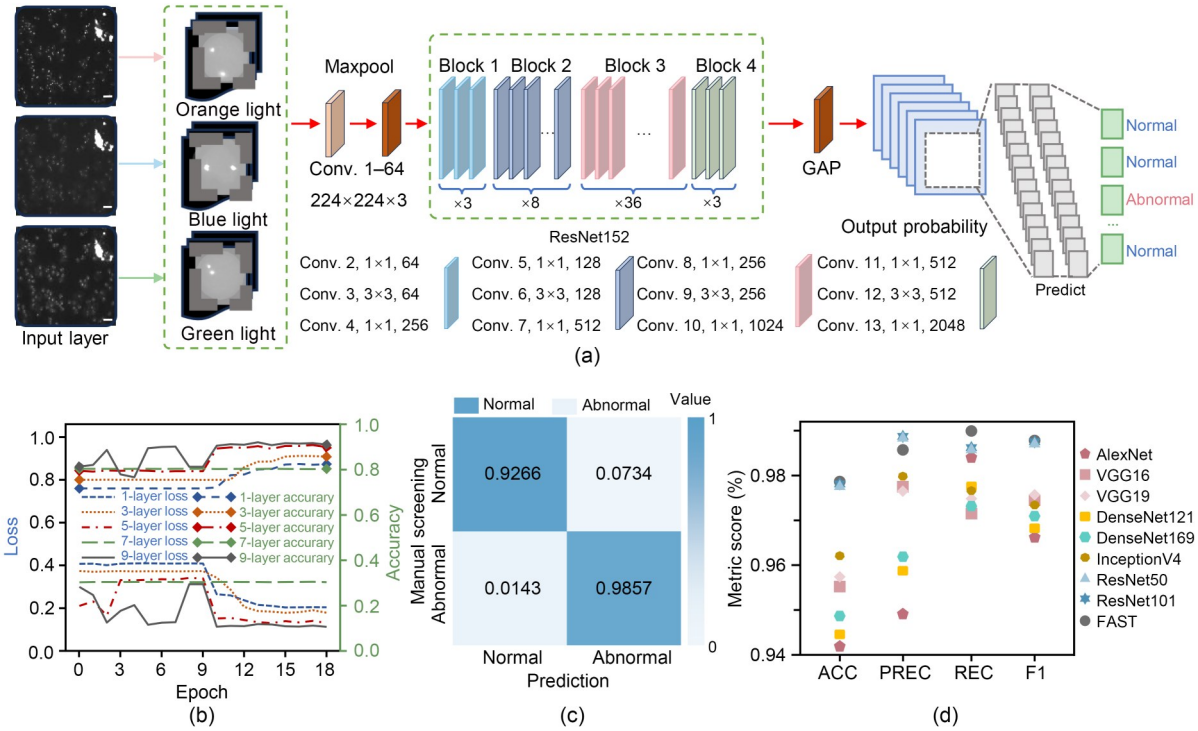

Fig. 5 Deep-learning-based cell abnormality detection and cancer diagnosis: (a) CNN ResNet152 network architecture for automated cell abnormality classification; (b) learning curves of the ResNet152 network trained on datasets with different fusion depths; (c) confusion matrix comparing ResNet152-based predictions with manual screening across 10 samples; (d) performance comparison between our method and eight representative deep learning models. Conv. is the abbreviation of convolution; ACC, PREC, REC, and F1 denote accuracy, precision, recall, and F1-score, respectively. Scale bars: 50 μm in (a)

usability and interpretability, the system overlays chromosomal pattern masks onto segmented nucleus boundaries, with orange and blue indicating positive and negative cases, respectively (Fig. S16 of the ESM). The precision rate generally remains between 0.95 and 1.00, indicating that the model has a low false-positive rate and strong classification ability. It showed significant accuracy and robustness in detecting cell abnormalities and CLL-positive diagnoses across diverse patient datasets, providing a robust solution to mitigate errors associated with manual detection. The model robustness was further validated through benchmarking against eight state-of-the-art deep learning algorithms using identical training and validation datasets: AlexNet (Battleday et al., 2020), VGG16 (Li et al., 2020), VGG19 (Le Goallec et al., 2022), ResNet50 (Zheng et al., 2022), ResNet101 (Ismael and Şengür, 2021), DenseNet121 (Singh et al., 2025), DenseNet169 (Biancalani et al., 2021), and InceptionV4 (Li FD et al., 2022). Our ResNet152-based model, i.e., FAST, achieved the highest cancer-detection accuracy of 97.86% (Fig. S17 of the ESM), outperforming all benchmarked methods and demonstrating strong clinical diagnostic potential. It also surpassed commercial AI-based systems across multiple metrics, including the accuracy, precision, recall, and F1-score (Fig. 5d). Unlike end-to-end commercial solutions, first, a refined segmentation algorithm is employed to delineate nucleus boundaries, effectively addressing challenges such as indistinct contours and overlapping nuclei. Second, a classification algorithm is applied to detect chromosomal abnormalities within the segmented regions. This dual approach minimizes false positives and improves sensitivity, ensuring robust performance across complex datasets.

To efficiently identify and visualize cell abnormalities, the system locates the nuclei with assigned chromosomal patterns and superimposes corresponding nucleus masks over the nucleus boundaries (Fig. 6a and Tables S8–S10 of the ESM). To further reduce the time and cost required for personnel training and operation, these functionalities are fully integrated

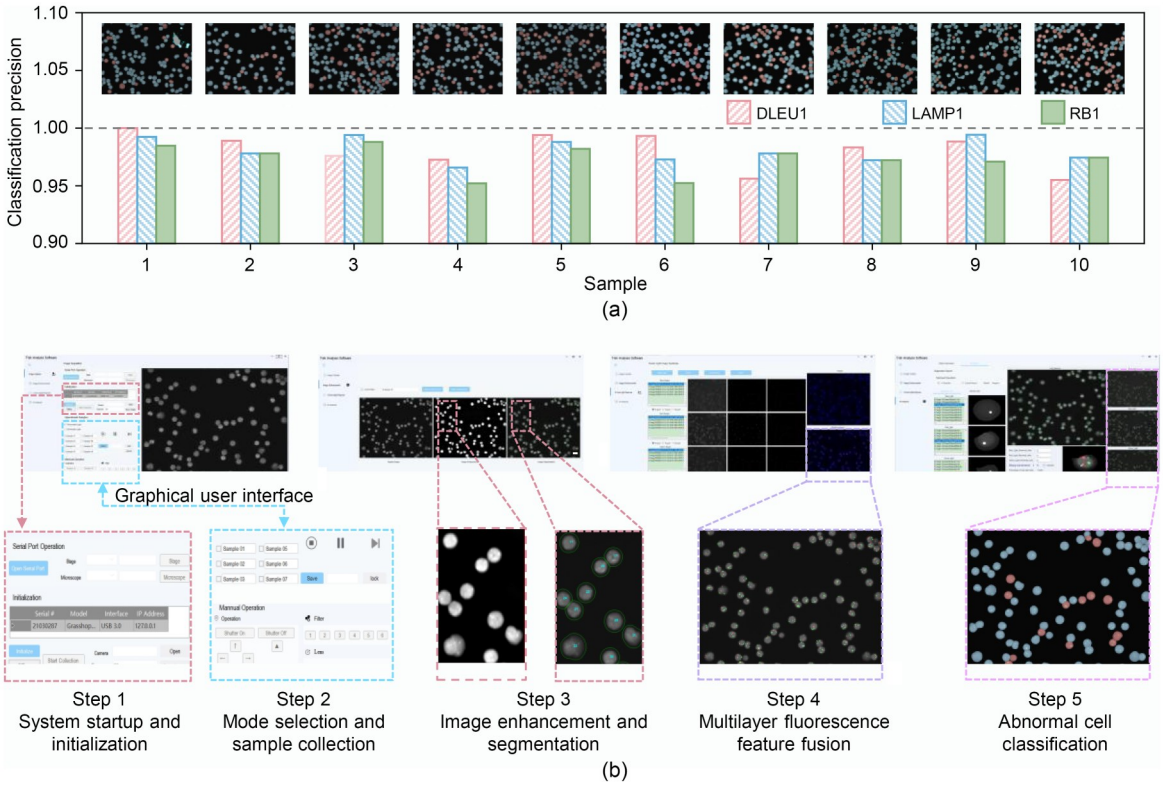

Fig. 6 Abnormality analysis results and system GUI: (a) classification precision of chromosomal abnormality involving tricolor fluorescence probes using the ResNet152 CNN network; (b) visualization of GUI and diagnostic report of the integrated FISH imaging and analysis system, tailored for non-experts and facilitating early cancer diagnosis and prognostic evaluation. Insets in (a) show microscopic sample images with color masks, where orange and blue indicate abnormality and normality, respectively. Scale bars: 50 μm in (a) and (b)

into a comprehensive multiplexed FAST designed for early cancer diagnosis (Fig. 6b and Section S10 of the ESM). The platform features a user-friendly graphical user interface (GUI) that simplifies operation by supporting real-time monitoring of image acquisition and processing, adjustable imaging parameters, and flexible program execution. This enables users to automate key tasks, including image acquisition, nucleus and fluorescence signal processing, AI-driven abnormality analysis, and diagnostic report generation (Table S11 of the ESM). Further, the system supports both automated and manual segmentation adjustments to meet diverse analytical requirements. The entire workflow, from image acquisition to report generation, can be completed within 45 min (Table S12 of the ESM) on a common computer. By integrating cost-effective microscopy, targeted fluorescent probes, and optimized FISH protocols, the FAST platform provides a reliable, rapid, and cost-effective solution for cellular abnormality detection, advancing early cancer diagnostics.

4 Conclusions

In this paper, we have introduced an automated and multiplexed FAST tailored for diagnosing CLL. The system comprises four core functionalities: automated image acquisition, image enhancement and nucleus segmentation, multilayer fluorescence feature fusion, and AI-driven chromosomal and cell nucleus abnormality detection. During image acquisition, FAST automatically selects the clearest image layers, effectively minimizing imaging artifacts. Nuclei contours are refined through imaging enhancement and segmentation, while multilayer fluorescence feature fusion enhances the cytogenetic information necessary for detecting cell abnormalities. Our segmentation and abnormality detection models outperform traditional methods, even in challenging regions with overlapping or densely packed nuclei. In terms of efficiency, FAST achieves accuracy and data richness comparable to commercial software while requiring

fewer computational resources and smaller sample sizes. The entire process, from image capture to analysis, can be completed within 45 min, significantly improving the speed, accuracy, and reliability of genetic analysis.

A standout feature of the FAST platform lies in its ability to identify abnormalities in densely packed nuclei, overcoming challenges commonly encountered by commercial methods. The seamless integration of automated segmentation and fluorescence feature fusion enables the precise detection of chromosomal and cellular abnormalities, which is critical for early cancer detection. Its GUI further enhances accessibility for non-expert users, facilitating intuitive image processing, analysis, and interpretation. Collectively, FAST provides a transformative and scalable solution for early cancer detection and personalized healthcare. We plan to further refine the deep learning models and extend the platform's capabilities to accommodate larger and more complex datasets, thereby broadening its applicability to other diseases and biological scales, ranging from single cells to tissues (Ueda et al., 2020). Ultimately, the FAST aims to support personalized treatment strategies, enhance prognostic evaluations, and improve patient outcomes through fast, accurate, and automated genetic analysis.

Despite leveraging deep learning techniques for accurate detection, several limitations remain in the current study:

1) Model interpretability: although the ResNet152-based model exhibits excellent diagnostic accuracy, its interpretability remains limited. Clinicians may require clearer visualization and explanation of how the model arrives at diagnostic conclusions, which is essential for building trust and integrating AI tools into clinical workflows.

2) Multi-target detection and complex genomic contexts: the current implementation focuses mainly on the 13q14 deletion associated with CLL. Expanding the system to accurately detect multiple genetic abnormalities simultaneously remains a challenge, particularly in complex genomic contexts, where overlapping signals or structural variants may interfere with probe interpretation.

3) Dataset diversity and scale: the model was validated on 100 clinical CLL cases. Although results were consistent with expert interpretations, larger and more diverse datasets covering different cancer types, imaging modalities, and staining conditions are necessary to further improve model robustness and generalizability.

4) Hardware and imaging constraints: while FAST is designed to operate with standard wide-field fluorescence microscopy, imaging performance may vary with hardware configurations, optical alignment, or sample preparation quality, which could affect reproducibility across institutions.

Building on these findings, our future efforts will focus on several key directions:

I) Enhancing model explainability: integrating attention heatmaps, gradient-weighted class activation mapping (Grad-CAM), or shapley additive explanation (SHAP)-based visualization to provide interpretable diagnostic reasoning and strengthen clinician confidence.

II) Extending multi-target and multi-cancer detection: developing adaptive probe designs and multi-class classification frameworks to enable simultaneous detection of multiple chromosomal abnormalities across diverse cancer types such as breast, cervical, and pancreatic cancers.

III) Scaling clinical validation: expanding clinical trials with large multi-center datasets to validate system reliability under diverse imaging and genetic conditions, ensuring the system's translational applicability in real-world hospital environments.

IV) Optimizing real-time processing: incorporating GPU-accelerated inference and cloud-based computation to achieve near real-time diagnostic feedback, enhancing throughput and integration with digital pathology systems.

V) Integrating multi-modal data: combining FISH imaging data with next-generation sequencing and histopathological features to build a hybrid diagnostic model that supports comprehensive precision oncology.

Acknowledgments

This work is supported by the Science and Technology Development Plan of Jilin Province (No. 20240404052ZP), China, and the Fundamental Research Funds for the Central Universities (No. QTZX23063), China. The authors would also like to acknowledge the staff of Zhongshan Hospital affiliated to Fudan University, Shanghai, China, for their support and cooperation.

Author contributions

Lemin SHI, Yuqiang ZHANG, and Xin FENG: conceptualization; Lemin SHI, Chengyue LU, and Xin FENG:

methodology; Lemin SHI, Haoyu QI, and Dianxin SONG: software; Lemin SHI and Yuqiang ZHANG: validation; Ping GONG and Chengyue LU: formal analysis; Menglei HU, Mingye LI, and Hao ZHANG: investigation; Ping GONG and Xin FENG: resources; Hao ZHANG and Shan JIANG: data curation; Lemin SHI, Shan JIANG, and Yuqiang ZHANG: writing–original draft; Lemin SHI, Xin FENG, and Shan JIANG: writing–review and editing; Lemin SHI: visualization; Xin FENG and Shan JIANG: supervision; Lemin SHI, Yuqiang ZHANG, and Hao ZHANG: project administration; Ping GONG, Xin FENG, and Shan JIANG: funding acquisition. All authors have read and agreed to the published version of the manuscript.

Conflict of interest

Lemin SHI, Yuqiang ZHANG, Haoyu QI, Chengyue LU, Menglei HU, Mingye LI, Dianxin SONG, Hao ZHANG, Xin FENG, Ping GONG, and Shan JIANG declare no conflict of interest.

References

Abrol V, Dhalla S, Gupta S, et al., 2023. An automated segmentation of leukocytes using modified watershed algorithm on peripheral blood smear images. *Wireless Personal Communications*, 131(1):197-215. https://doi.org/10.1007/s11277-023-10424-1

Battleday RM, Peterson JC, Griffiths TL, 2020. Capturing human categorization of natural images by combining deep networks and cognitive models. *Nature Communications*, 11(1):5418. https://doi.org/10.1038/s41467-020-18946-z

Biancalani T, Scalia G, Buffoni L, et al., 2021. Deep learning and alignment of spatially resolved single-cell transcriptomes with tangram. *Nature Methods*, 18(11):1352-1362. https://doi.org/10.1038/s41592-021-01264-7

Caicedo JC, Cooper S, Heigwer F, et al., 2017. Data-analysis strategies for image-based cell profiling. *Nature Methods*, 14(9):849-863. https://doi.org/10.1038/nmeth.4397

Choudhary G, Sethi D, 2023. Mathematical modeling and simulation of multi-focus image fusion techniques using the effect of image enhancement criteria: a systematic review and performance evaluation. *Artificial Intelligence Review*, 56(11):13787-13839. https://doi.org/10.1007/s10462-023-10487-3

Chyad M, Zaidan BB, Zaidan AA, et al., 2025. Exploring adversarial deep learning for fusion in multi-color channel skin detection applications. *Information Fusion*, 114: 102632. https://doi.org/10.1016/j.inffus.2024.102632

Cui J, Liu YT, Lv R, et al., 2024. Fluorescence in situ hybridization reveals the evolutionary biology of minor clone of gain/amp(1q) in multiple myeloma. *Leukemia*, 38(6): 1299-1306. https://doi.org/10.1038/s41375-024-02237-3

Dai Y, Idorn M, Serrero MC, et al., 2024. TMEFF1 is a neuron-specific restriction factor for herpes simplex virus. *Nature*, 632(8024):383-389. https://doi.org/10.1038/s41586-024-07670-z

Durak Aras B, Isik S, Uskudar Teke H, et al., 2021. Which prognostic marker is responsible for the clinical heterogeneity in CLL with 13q deletion? *Molecular Cytogenetics*, 14(1):2. https://doi.org/10.1186/s13039-020-00522-1

Elkrief A, Montesion M, Sivakumar S, et al., 2024. Intratumoral escherichia is associated with improved survival to single-agent immune checkpoint inhibition in patients with advanced non-small-cell lung cancer. *Journal of Clinical Oncology*, 42(28):3339-3349. https://doi.org/10.1200/jco.23.01488

Hu CS, Li H, Ma T, et al., 2024. An improved image enhancement algorithm: radial contrast-limited adaptive histogram equalization. *Multimedia Tools and Applications*, 83(36):83695-83707. https://doi.org/10.1007/S11042-024-18922-5

Hu Y, Jones D, Zhao WQ, et al., 2023. Incidence, clinicopathologic features, *HER2* fluorescence in situ hybridization profile, and oncotype DX results of human epidermal growth factor receptor 2-low breast cancers: experience from a single academic center. *Modern Pathology*, 36(7):100164. https://doi.org/10.1016/j.modpat.2023.100164

Huber D, Voith von Voithenberg L, Kaigala GV, 2018. Fluorescence in situ hybridization (FISH): history, limitations and what to expect from micro-scale FISH? *Micro and Nano Engineering*, 1:15-24. https://doi.org/10.1016/j.mne.2018.10.006

Ismael AM, Şengür A, 2021. Deep learning approaches for COVID-19 detection based on chest X-ray images. *Expert Systems with Applications*, 164:114054. https://doi.org/10.1016/j.eswa.2020.114054

Jardim S, António J, Mora C, 2022. Graphical image region extraction with K-means clustering and watershed. *Journal of Imaging*, 8(6):163. https://doi.org/10.3390/jimaging8060163

Jonkman J, Brown CM, Wright GD, et al., 2020. Tutorial: guidance for quantitative confocal microscopy. *Nature Protocols*, 15(5):1585-1611. https://doi.org/10.1038/s41596-020-0313-9

Knöll M, Dheenadayalan RP, Yosifov DY, et al., 2024. Biallelic deletion 13q in chronic lymphocytic leukemia treated with targeted agents. *Blood*, 144(S1):4608. https://doi.org/10.1182/blood-2024-204910

Krayem B, Moustafa-Hawash N, Frisch A, et al., 2024. Optical genome mapping reclassifies patients with intermediate risk acute myeloid leukemia. *Blood*, 144(S1):1559. https://doi.org/10.1182/blood-2024-206768

Lankford A, Swaminathan M, Gonugunta AS, et al., 2024. Predictors for time-to-first-treatment in patients with del (17p) and/or *TP53*-mutated chronic lymphocytic leukemia. *Blood*, 144(S1):3246. https://doi.org/10.1182/blood-2024-208974

Le Goallec A, Diai S, Collin S, et al., 2022. Using deep learning

to predict abdominal age from liver and pancreas magnetic resonance images. *Nature Communications*, 13(1):1979. https://doi.org/10.1038/s41467-022-29525-9

Lewis SM, Asselin-Labat ML, Nguyen Q, et al., 2021. Spatial omics and multiplexed imaging to explore cancer biology. *Nature Methods*, 18(9):997-1012. https://doi.org/10.1038/s41592-021-01203-6

Li DG, Bledsoe JR, Zeng Y, et al., 2020. A deep learning diagnostic platform for diffuse large B-cell lymphoma with high accuracy across multiple hospitals. *Nature Communications*, 11(1):6004. https://doi.org/10.1038/s41467-020-19817-3

Li FD, Yang YQ, Wei YN, et al., 2022. Predicting neoadjuvant chemotherapy benefit using deep learning from stromal histology in breast cancer. *npj Breast Cancer*, 8(1):124. https://doi.org/10.1038/s41523-022-00491-1

Li PY, Tian JD, Tang YD, et al., 2021. Deep retinex network for single image dehazing. *IEEE Transactions on Image Processing*, 30:1100-1115. https://doi.org/10.1109/tip.2020.3040075

Li XJ, Hou GJ, Li KQ, et al., 2022. Enhancing underwater image via adaptive color and contrast enhancement, and denoising. *Engineering Applications of Artificial Intelligence*, 111:104759. https://doi.org/10.1016/j.engappai.2022.104759

Li YZ, Pillar N, Li JX, et al., 2024. Virtual histological staining of unlabeled autopsy tissue. *Nature Communications*, 15(1):1684. https://doi.org/10.1038/s41467-024-46077-2

Malik H, Naeem A, Sadeghi-Niaraki A, et al., 2024. Multi-classification deep learning models for detection of ulcerative colitis, polyps, and dyed-lifted polyps using wireless capsule endoscopy images. *Complex & Intelligent Systems*, 10(2):2477-2497. https://doi.org/10.1007/s40747-023-01271-5

Minaee S, Boykov Y, Porikli F, et al., 2022. Image segmentation using deep learning: a survey. *IEEE Transactions on Pattern Analysis and Machine Intelligence*, 44(7):3523-3542. https://doi.org/10.1109/tpami.2021.3059968

Nasir ES, Parvaiz A, Fraz MM, 2023. Nuclei and glands instance segmentation in histology images: a narrative review. *Artificial Intelligence Review*, 56(8):7909-7964. https://doi.org/10.1007/s10462-022-10372-5

Ordoñez R, Zhang WM, Ellis G, et al., 2024. Genomic context sensitizes regulatory elements to genetic disruption. *Molecular Cell*, 84(10):1842-1854.e7. https://doi.org/10.1016/j.molcel.2024.04.013

Otomo K, Omura T, Nozawa Y, et al., 2024. descSPIM: an affordable and easy-to-build light-sheet microscope optimized for tissue clearing techniques. *Nature Communications*, 15(1):4941. https://doi.org/10.1038/s41467-024-49131-1

Patino T, 2024. Imaging DNA origami by fluorescence in situ hybridization. *Nature Nanotechnology*, 19(1):1-2. https://doi.org/10.1038/s41565-023-01556-3

Perez-Lopez R, Ghaffari Laleh N, Mahmood F, et al., 2024. A guide to artificial intelligence for cancer researchers. *Nature Reviews Cancer*, 24(6):427-441. https://doi.org/10.1038/s41568-024-00694-7

Plass M, Kargl M, Kiehl TR, et al., 2023. Explainability and causability in digital pathology. *The Journal of Pathology: Clinical Research*, 9(4):251-260. https://doi.org/10.1002/cjp2.322

Punn NS, Agarwal S, 2022. Modality specific U-Net variants for biomedical image segmentation: a survey. *Artificial Intelligence Review*, 55(7):5845-5889. https://doi.org/10.1007/s10462-022-10152-1

Ramos-Soto O, Rodríguez-Esparza E, Balderas-Mata SE, et al., 2021. An efficient retinal blood vessel segmentation in eye fundus images by using optimized top-hat and homomorphic filtering. *Computer Methods and Programs in Biomedicine*, 201:105949. https://doi.org/10.1016/j.cmpb.2021.105949

Saeed N, Khan ZF, Jehanzeb H, et al., 2024. Frequency of deletion 13q14.3 and its impact on outcome in patients of chronic lymphocytic leukemia: a single-centered institutional study from pakistan. *Journal of Haematology and Stem Cell Research*, 4(1):120-124.

Schermelleh L, Ferrand A, Huser T, et al., 2019. Super-resolution microscopy demystified. *Nature Cell Biology*, 21(1):72-84. https://doi.org/10.1038/s41556-018-0251-8

Scott DW, King RL, Staiger AM, et al., 2018. High-grade B-cell lymphoma with *MYC* and *BCL2* and/or *BCL6* rearrangements with diffuse large B-cell lymphoma morphology. *Blood*, 131(18):2060-2064. https://doi.org/10.1182/blood-2017-12-820605

Sharma AK, Nandal A, Dhaka A, et al., 2022. Enhanced watershed segmentation algorithm-based modified ResNet50 model for brain tumor detection. *BioMed Research International*, 2022:7348344. https://doi.org/10.1155/2022/7348344

Shen X, Qi YF, Ma TF, et al., 2019. A dicentric chromosome identification method based on clustering and watershed algorithm. *Scientific Reports*, 9(1):2285. https://doi.org/10.1038/s41598-019-38614-7

Sheng G, Hu G, Wang X, et al., 2025. Cross-layer frequency-spatial domain feature interaction awareness fusion for fine-grained visual classification. *Information Fusion*, 103788. https://doi.org/10.1016/j.inffus.2025.103788

Siegel RL, Miller KD, Wagle NS, et al., 2023. Cancer statistics, 2023. *CA: A Cancer Journal for Clinicians*, 73(1):17-48. https://doi.org/10.3322/caac.21763

Siegel RL, Giaquinto AN, Jemal A, 2024. Cancer statistics, 2024. *CA: A Cancer Journal for Clinicians*, 74(1):12-49. https://doi.org/10.3322/caac.21820

Singh Y, Eaton JE, Venkatesh SK, et al., 2025. Deep learning analysis of MRI accurately detects early-stage perihilar cholangiocarcinoma in patients with primary sclerosing cholangitis. *Hepatology*, 83(1):30-39. https://doi.org/10.1097/hep.0000000000001314

Skerget S, Penaherrera D, Chari A, et al., 2024. Comprehensive molecular profiling of multiple myeloma identifies refined copy number and expression subtypes. *Nature Genetics*, 56(9):1878-1889. https://doi.org/10.1038/s41588-024-01853-0

Soltanian-Zadeh S, Sahingur K, Blau S, et al., 2019. Fast and robust active neuron segmentation in two-photon calcium imaging using spatiotemporal deep learning. *Proceedings of the National Academy of Sciences of the United States of America*, 116(17):8554-8563. https://doi.org/10.1073/pnas.1812995116

Sun LJ, Ke XD, Guan A, et al., 2023. Intratumoural microbiome can predict the prognosis of hepatocellular carcinoma after surgery. *Clinical and Translational Medicine*, 13(7):e1331. https://doi.org/10.1002/ctm2.1331

Sun Y, Zhao ZC, Jiang D, et al., 2022. Low-illumination image enhancement algorithm based on improved multi-scale retinex and ABC algorithm optimization. *Frontiers in Bioengineering and Biotechnology*, 10:865820. https://doi.org/10.3389/fbioe.2022.865820

Syrykh C, van den Brand M, Kather JN, et al., 2025. Role of artificial intelligence in haematolymphoid diagnostics. *Histopathology*, 86(1):58-68. https://doi.org/10.1111/his.15327

Tao YF, Zhou XL, Sun LQ, et al., 2023. Highly efficient and robust π-FISH rainbow for multiplexed in situ detection of diverse biomolecules. *Nature Communications*, 14(1):443. https://doi.org/10.1038/s41467-023-36137-4

Teierle SM, Huang Y, Kittai AS, et al., 2023. Characteristics and outcomes of patients with CLL and *CDKN2A/B* deletion by fluorescence in situ hybridization. *Blood Advances*, 7(23):7239-7242. https://doi.org/10.1182/bloodadvances.2023010753

Ueda HR, Ertürk A, Chung K, et al., 2020. Tissue clearing and its applications in neuroscience. *Nature Reviews Neuroscience*, 21(2):61-79. https://doi.org/10.1038/s41583-019-0250-1

Vincent L, Dougherty ER, 1994. Morphological segmentation for textures and particles. *In*: Dougherty ER (Ed.), Digital Image Processing Methods. CRC Press, Boca Raton, USA, p.43-102. https://doi.org/10.1201/9781003067054

Wang L, You ZH, Lu W, et al., 2024. Attention-aware sobel graph convolutional network for remote sensing image change detection. *IEEE Transactions on Geoscience and Remote Sensing*, 62:4409912. https://doi.org/10.1109/TGRS.2024.3419790

Xie XY, Cui Q, Jiang TT, et al., 2024. A critical role of the endothelial S-phase kinase-associated protein 2/phosphatase and tensin homologue axis in angiogenesis and psoriasis. *British Journal of Dermatology*, 190(2):244-257. https://doi.org/10.1093/bjd/ljad399

Xu LS, Zhang HR, Wang JL, et al., 2023. Information loss challenges in surgical navigation systems: from information fusion to AI-based approaches. *Information Fusion*, 92:13-36. https://doi.org/10.1016/j.inffus.2022.11.015

Zhang B, Qiu LY, Xiao W, et al., 2021. Reconstruction of the hypothalamo-neurohypophysial system and functional dissection of magnocellular oxytocin neurons in the brain. *Neuron*, 109(2):331-346.e7. https://doi.org/10.1016/j.neuron.2020.10.032

Zhang RH, Khare P, Banerjee P, et al., 2024. The *DLEU2/miR-15a/miR-16-1* cluster shapes the immune microenvironment of chronic lymphocytic leukemia. *Blood Cancer Journal*, 14(1):168. https://doi.org/10.1038/s41408-024-01142-3

Zhao ZJ, Yang WB, Kong R, et al., 2023. CircEIF3I facilitates the recruitment of SMAD3 to early endosomes to promote TGF-β signalling pathway-mediated activation of MMPs in pancreatic cancer. *Molecular Cancer*, 22(1):152. https://doi.org/10.1186/s12943-023-01847-2

Zheng HD, Sun YL, Kong DW, et al., 2022. Deep learning-based high-accuracy quantitation for lumbar intervertebral disc degeneration from MRI. *Nature Communications*, 13(1):841. https://doi.org/10.1038/s41467-022-28387-5

Zhong GL, Zhao Q, Chen ZL, et al., 2023. TGF-β signaling promotes cervical cancer metastasis via CDR1as. *Molecular Cancer*, 22(1):66. https://doi.org/10.1186/s12943-023-01743-9

Electronic Supplementary materials

Sections S1–S10, Figs. S1–S17, Tables S1–S12